JJEES

JJEES (2026) 17 (3): 311-323
ISSN 1995-6681

Jordan Journal of Earth and Environmental Sciences

Surface Temperature and Evaporation Rates across the Gulf of Aqaba as Investigated from Landsat and Modis Data

Ibrahim M. Oroud* and Sattam Salem AlShogoor

Mutah University, Karak, Jordan

Received on 19 November 2025; Accepted on 12 March 2026

Abstract

Monthly surface temperature (ST) and evaporation rates across the Gulf of Aqaba (GOA) were derived using thermal images from Landsat 8 and near-surface meteorological data. Retrieved ST were compared with surface temperature from MODIS data for the same period, and both sets yielded similar results. Surface temperature of the GOA showed little annual range, with a minimum of ~20 ^{O}C in March and a maximum of 27 ^{O}C in August and September. However, the annual temperature range across the GOA is not uniform, varying from ~5.6 ^{O}C in the southern parts to ~9 ^{O}C in the northern parts, reflecting the flow regime from the Red Sea and the climate conditions across the GOA.

Average annual evaporation rate across the GOA, as calculated with the Penman equation, is ~2860 mm, giving a net water balance deficit for the entire GOA of ~ 8.8×10^9 m^3 annually. This deficit is compensated primarily via water flux from the Red Sea. Evaporation during April through September accounts for ~ one half of annual evaporation while the other half occurs during October through March. This evaporation characteristic is linked to the very large heat storage during the warming phase and its subsequent release in the cooling period of the annual cycle. A small evaporation gradient is noticed across the GOA, being more distinct in the cold season. The aerodynamic term represents a significant portion of evaporation during the low sun period, accounting for ~56% of total evaporation during December through February and ~28% from July through September. The annual trend of evaporation partitioning between energy and aerodynamic terms is attributed to the evaporation conversion efficiency of net radiation which increases as temperature increases. Thermal images have the potential to provide accurate measurements of surface temperature that can be used to understand climate dynamics and water balance across large spatial domains.

Keywords: *Gulf of Aqaba, evaporation rates, thermal images, atmospheric correction, marine environments*

1. Introduction

Evaporation is a crucial geophysical component of the energy and hydrological cycle over the Earth's surface. Around 77% of net radiation is dissipated via evaporation on a global scale (Budyko, 1974; Vonder Haar, 1994). The transformation of water from the liquid to the gaseous phase requires a large input of energy, and 2.45 MJ is needed to evaporate 1 kg of water. Unlike many other atmospheric elements, such as wind speed, air temperature, and relative humidity, which can directly be measured, evaporation is a derived element, and its rate is an integrated function of numerous interrelated surface elements and atmospheric forcings (Brutsaert, 1982; Allen et al., 1998; Foken, 2008). Until recently, sea surface temperature and turbulent fluxes were measured using conventional methods such as offshore sites and floating buoys to evaluate the annual cycle of temperature and spatial distribution of heat and mass transport across the sea-atmosphere interface (Stammer et al., 2002; Reynolds and Chelton, 2010; Gristey et al., 2021). These measurements provided valuable information of the spatial distribution of SST and vertical turbulent fluxes over the various parts of the world oceans (Vonder Haar, 1994; Kelkar, 2007). Although very informative and providing valuable background data, field campaigns are usually confined to point measurements, costly, and require large logistical investments. Furthermore, the spatial distribution of SST and turbulent fluxes obtained using field campaigns is deduced by interpolation rather than by direct measurements, entailing substantial smoothing and data approximation. The launch of satellites equipped with sensors having high spectral, radiometric, and spatial resolutions, along with their large synoptic scenes and relatively short time revisits, has revolutionized data gathering methods (Qin et al., 2001; Wang et al., 2015; Cristobal et al., 2018). Sensors onboard satellites can capture a large scene instantaneously, allowing for direct evaluation of processes in a static time domain (Sobrino et al., 2018; Diaz et al., 2021; Oroud, 2022; Oroud, 2025). Numerous investigators indicated that thermal satellite images yield high quality surface temperature with excellent spatial and temporal resolutions (Qin et al., 2001; Jimenez-Munoz and Sobrino, 2003; Jimenez-Munoz et al., 2014). The accuracy of atmospherically corrected surface temperature has been reported to be less than 1 K in relatively dry atmospheres with water vapor content below 2 g (Qin et al., 2003; Jiménez-Muñoz et al., 2009; Sobrino et al., 2018).

The Gulf of Aqaba (hereafter GOA), which represents

* Corresponding author e-mail: ioroud@mutah.edu.jo

the northern flank of the Red Sea, has received considerable attention due to its unique ecological habitats, the widespread tourist activity, the presence of numerous desalination projects and for understanding temperature structure, turbulent fluxes and water exchange with the Red Sea (Manasrah et al., 2006; 2019; Biton and Gildor, 2011; Ahmed et al., 2012; Faraj et al., 2022). Numerous studies were conducted in the GOA and the Red Sea to assess the energy budget, salinity, turbulent fluxes, and water exchange with the open seas (Assaf and Kessler, 1976; Paldor and Anati, 1979; Matsoukas et al., 2005; 2007).

The earliest attempt to assess evaporation from the GOA and the Red Sea was carried out by Neumann (1952) who indicated that evaporation rates were in the range 2000 mm a^{-1} in the GOA at 29^{O} N to 2350 mm a^{-1} in the southern parts of the Red Sea ~ 15^{O} N. Assaf and Kessler (1976) evaluated the annual flux of evaporation from the GOA based on hourly data collected in two sites situated in the northern parts of the GOA and indicated that evaporation was close to 3600 mm a^{-1}. Paldor and Anati (1979) investigated the monthly distribution of temperature and salinity across the GOA based on observations collected from 1974 through 1977 at nine sites distributed along the GOA. They found that surface temperature and salinity were high in summer ~26 ^{O}C, and 41 g kg^{-1} and low in winter ~21 ^{O}C and 40.5 g kg^{-1}.

Other relevant investigations were carried out in the Red Sea to assess turbulent fluxes across its surface; thus, the results obtained in this area are expected to be close to those encountered over the GOA because of the relative similarity in climate conditions. For instance, da Salva et al (1994) reported that the evaporation rate from the Red Sea is close to 1680 mm a^{-1}. Using a coarse spatial resolution of 2.5 × 2.5 degrees, Matsoukas et al (2007) indicated that evaporation over the Red Sea is ~2120 mm a^{-1} (see also Matsoukas et al., 2005). Based on the Penman equation, Dehwaha et al (2016) reported that evaporation from the Red Sea was close to 2600 mm a^{-1}. Numerous assumptions were made by the various investigators to reach the estimates presented above, such as the homogeneity of surface temperature and uniform weather conditions across the study sites. Furthermore, the various investigators did not take into account the suppression of evaporation caused by the salinity of seawater (e.g., Calder and Neal, 1984; Oroud, 2019a; Oroud, 2023). Thus, the objective of the present investigation is to examine the annual cycle of surface temperature and evaporation rates across the GOA using thermal images onboard Landsat 8 during the period February 2020 through January 2021. Surface temperatures retrieved from Landsat were compared with their corresponding values obtained from MODIS data. The present investigation is important for understanding the annual cycle of the sea surface thermal regime and the energy budget partitioning in a hyperarid marine environment, as well as for assessing water flux from the Red Sea.

2. Study area

The GOA forms the southern end of the Dead Sea Transform, created by the Sinai Peninsula's bifurcation of the northern Red Sea (Biton and Gildor, 2011). The Gulf of Suez occupies the western flank, while the GOA occupies the eastern one (Figure 1). The study area is located between 34.4 - 34.96 E and between 28 - 29.54 N. The north-south extension of the GOA is ~ 180 km, and its maximum width is ~ 28 km, with an area close to 3100 km^2. The gulf is semi-closed with an average depth of 800 m and a maximum depth reaching 1800 m (Biton and Gildor, 2011). This elongated, narrow gulf is an important marine site hosting unique assemblages of ecological habitats and supports a well-known coral reef ecosystem.

The GOA is situated in a hyperarid climate zone, and annual precipitation ranges from 20 to 30 mm a^{-1}, with some years passing without a single rainy event. Being located in a permanent subtropical high- pressure zone, the GOA receives substantial amounts of solar radiation year-round. Air temperature closely tracks solar radiation receipt, with average monthly air temperature varying from 15°C in January to 33°C in July and August.

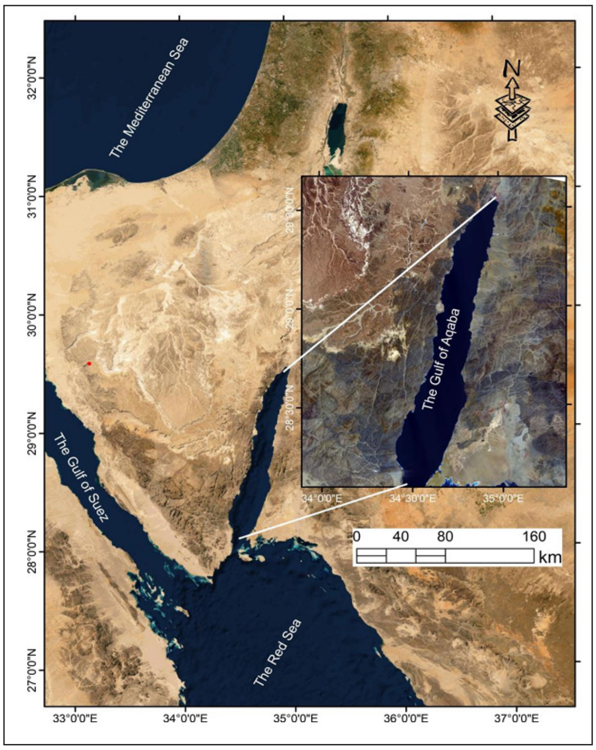

Figure 1. Location of the study area. The inset map is a pan-sharpened image taken in April 2020, showing the Gulf of Aqaba and surrounding terrain in greater detail.

3. Data and methods

A flowchart of the data requirements and processes involved in obtaining surface temperatures and evaporation rates across the GOA is presented in Figure 2. The first step was to estimate the kinetic temperature of the study area. After that, a series of processes were carried out to generate raster layers- e.g., incoming longwave radiation, solar radiation, upwelling thermal radiation- needed to estimate evaporation across the study area. A detailed discussion of the generated elements is presented in the flowchart.

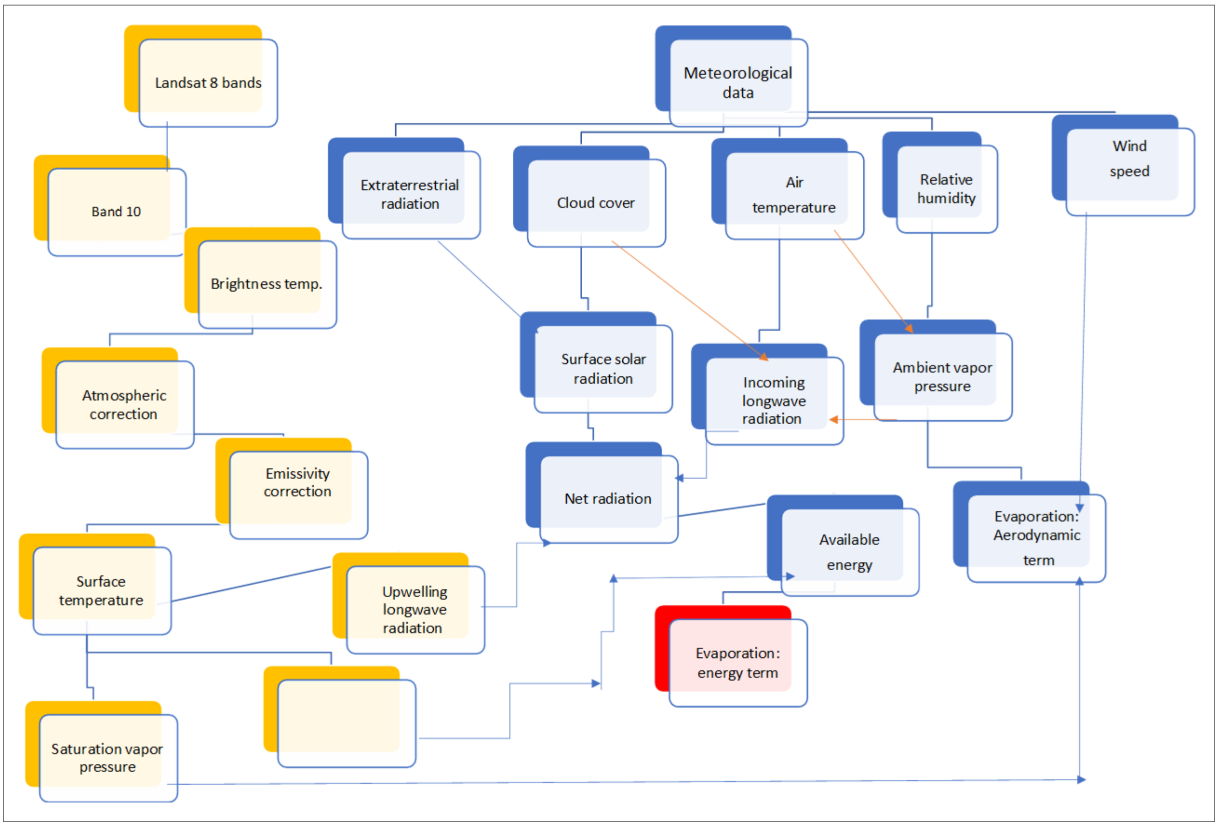

Figure 2. A flowchart showing data requirements and processes involved in obtaining surface temperature and evaporation across the GOA.

3.1 Meteorological data

Monthly meteorological data are obtained from archived data collected by the Department of Meteorology, Jordan, and from open sources. Solar radiation reaching the surface is evaluated from the extraterrestrial radiation and cloud cover observed in the northern tip of the Gulf. It is assumed that relative humidity, wind speed, and cloud cover over the GOA are well represented by observations in the northern parts, given the similarity in climate conditions across the study area. Table 1 displays the average monthly meteorological variables observed at the northern tip of the GOA.

Table 1. Average monthly weather conditions in the northern tip of the Gulf of Aqaba.

Month	So (MJ $m^2.day^{-1}$)	Ta (^oC)	RH (%)	U (m s-1)	C. cover (%)
J	14.88	15.0	53	6.0	23
F	18.96	16.7	45	6.0	22
M	23.45	20.0	37	6.7	20
A	27.00	24.4	30	6.7	23
M	29.15	28.9	29	6.9	19
J	29.95	31.7	31	7.5	3
J	29.61	33.3	33	7.1	2
A	28.11	33.3	38	7.1	1
S	25.32	31.1	44	6.8	2
O	21.43	27.2	47	5.9	13
N	17.43	21.7	48	5.9	24
D	14.65	16.7	53	5.8	27

3.2 Satellite data

3.2.1 Landsat data

8 OLI/TIRS has two thermal bands, 10 and 11, operating in the atmospheric window, 10-12.5 µm where atmospheric absorption and emission reach their minimum values. Band 10 operates in the spectral range 10.60–11.19 µm, with an effective wavelength of 10.904 µm, while band 11 operates in the spectral range 11.5-12.51 µm (Cristobal et al., 2018; Oroud and Balling, 2021). Thermal bands onboard Landsat 8 are captured at spatial and radiometric resolutions of 100 m and 12-bit, but are delivered to users at 30 m and 16-bit. Twelve images of the thermal band 10 covering the period February 2020 through January 2021, one for each month, were downloaded from the USGS site (https://earthexplorer.usgs.gov: path 174 Row 40). To ensure proper representation of surface temperature and to eliminate the influence of nearby terrain, the first 1 km along the shoreline was excluded.

3.2.2 MODIS data

Monthly SST from the Moderate Resolution Imaging Spectroradiometer (MODIS) onboard the Aqua satellite was downloaded for the study area from February 2020 through January 2021 to provide an independent check of the SST retrieved from band 10 onboard Landsat 8. MODIS sensors are sun-synchronous and flown on the NASA Terra and Aqua satellites, collecting imagery in 36 spectral bands for a wide range of applications in agriculture, forestry, meteorology, oceanography, and climate dynamics. This sensor is a key instrument designed as part of the Earth Observing System (EOS) to provide long-term global coverage of the Earth's land, ocean, and atmospheric properties. The MODIS SST product has high accuracy, with uncertainties of ~0.45 K at nadir and 0.56 K at 45°, as described in the Algorithm Technical Background Document (Brown and Minnett, 1999). This uncertainty range has been confirmed by other investigators (Qin et al., 2014; Ghanea et al., 2016; Cao et al., 2021). Thus, MODIS SST products can be used as a benchmark for SST validation. Retrieved SST was the average of daytime and nighttime readings, with a spatial resolution of 0.1 degree. All images were processed using ArcGIS Pro.

3.3 The brightness temperature

The spectral radiance emitted by a blackbody can be formulated using the Planck function (Menzel, 2006; Cristobal et al., 2018),

$$B\lambda(T) = \frac{hc^2}{\lambda^5 \mathrm{Exp}\left(\frac{hc}{\lambda kT}\right) - 1} \quad (1)$$

where Bλ(T) is the spectral radiance (W m^{-2} sr^{-1} μm^{-1}), λ is wavelength (μm), h is the Planck's constant (6.626076 × 10^{-34} J s), k is the Boltzmann's constant (1.380658× 10^{-23} J K^{-1}), T is the blackbody temperature, and c is the speed of light. Radiance impinging on a satellite sensor (L_{TOA}) is expressed as (Menzel, 2006),

$$L_{TOA} = \tau\epsilon L_S + l_U + \tau(1-\epsilon)L_D \quad (2)$$

where τ is atmospheric transmission (-), LS is radiation emitted by the surface, ε is surface emissivity in the specified band (-), L_D and L_U are downwelling and upwelling atmospheric radiation, respectively; all terms are expressed in (Wm^{-2} sr^{1} μm^{-1}). Thermal radiance at a satellite sensor is converted to a brightness temperature using the following form,

$$TB = \frac{K2}{\mathrm{Ln}\left(\frac{K1}{L\lambda}+1\right)} \quad (3)$$

where TB is the at sensor or brightness temperature, K1 and K2 are constants obtained from the Landsat 8 manual.

The actual surface temperature is different from the brightness temperature due to atmospheric and emissivity effects (Menzel, 2006; Cristobal et al., 2018). The temperature difference between the kinetic temperature and the brightness temperature could reach several degrees depending on atmospheric conditions and the actual emissivity across a scene (Qin et al., 2003; Menzel, 2006; Cristobal et al., 2018). Emissivity effect could be large for bare sandy dry surfaces, but it is relatively small for water surfaces because the spectral emissivity of water within the band used to retrieve surface radiance is close to unity (e.g., Menzel, 2006).

Due to absorption and remission of longwave radiation, the atmosphere influences the radiance received by a satellite sensor (e.g., Salisbury and D'Aria, 1992; Faysash and Smith, 1999). The temperature of the intervening atmosphere is usually lower than that of the surface, leading to a reduction in the recorded radiance at the sensor level (Barsi et al., 2005; Menzel, 2006; Rosas et al., 2017; Oroud, 2020). The kinetic temperature of the sea surface or that of a ground surface is higher than the brightness temperature. The effect of the atmosphere on the retrieved temperature depends primarily on the vertical structure of humidity and temperature within the lower troposphere (Parata, 1994; Qin et al., 2001; Wang et al., 2015; Cristobal et al., 2018; Diaz et al., 2021). Numerous techniques have been used to correct for the atmospheric effect such as the radiative transfer equation like MOTRAN, in situ measurements or empirical equations. The algorithm presented by Barsi et al (2005) to correct for the atmospheric effect is implemented in the present investigation (http://atmcorr.gsfc.nasa.gov.)

3.4 Evaporation calculation

Evaporation from a water surface can be estimated using a variety of methods, such as the pan ratio method, the bulk transfer method, the Penman- Priestly method, the combination equation, and the eddy covariance (Allen et al., 1998; Bouwer et al., 2007; Metzger et al., 2018; Oroud, 2019a). The bulk transfer method, which is widely used, is quite sensitive to the transfer coefficient and vapor pressure deficit across the surface- atmosphere boundary, and thus this method will give an evaporation that synchronizes closely with water temperature. The combination equation accounts for radiative, convective, and storage terms and is therefore expected to provide a better representation of the annual course of evaporation from a deep-water body like the GOA. The Penman equation is written (Mundo and Gomez, 2017; Oroud, 2019a),

$$E = \frac{\beta\Delta(RN+QS)+\Psi f(u)(\beta e_w - e_a)}{\beta\Delta+\Psi} \quad (4)$$

where E is evaporation (Wm^{-2}), β is the activity coefficient of the water surface (-), Δ is the slope of saturation vapor pressure with respect to temperature (hPa K^{-1}), RN is net radiation (W m^{-2}), QS is the change in heat storage (Wm^{-2}), ψ is the psychrometric constant (hPa K^{-1}), f(u) is the wind function (Wm^{-2} hPa^{-1}), e_w and ea are vapor pressure at the water surface and in the contiguous air (hPa). All parameters comprising the Penman equation are presented below.

The energy balance at the surface- atmosphere boundary may be expressed as (Foken, 2008; Oroud, 2023),

$$Rn = S(1-\alpha) + L\downarrow - L\uparrow \quad (5)$$

where Rn is net radiation (W m^{-2}), α is surface albedo (-), are incoming and outgoing longwave radiation. Monthly solar radiation is estimated from extraterrestrial radiation and cloud cover (Iqbal, 1982)

$$S_G = \left(a + b\frac{n}{N}\right) S_{Ext} \quad (6)$$

where SG is solar radiation reaching the surface, a and b are empirical constants, n and N are actual sunshine hours and the theoretical daylight length, S_{EXT} is the daily extraterrestrial solar radiation (MJ m^{-2} day^{-1}), computed using the following form (Iqbal, 1983),

$$S_{EXT} = S_C\, D(\sin\emptyset \sin\delta + \cos\emptyset \cos\delta \sin\omega) \quad (7)$$

where SC is the solar constant, D is the inverse earth-sun distance, Φ is latitude, δ is solar declination, and ω is the sunset angle.

Down-coming longwave radiation is estimated using an expression presented by Brutsaert (1982),

$$L\downarrow = \epsilon_a\, \sigma T_a^4 (1 + cc^{\gamma}) \tag{8}$$

where ε_a is atmospheric emissivity (-), σ is the Stefan-Boltzmann constant (5.667×10^{-8} $Wm^{-2}K^{-4}$), T_a is near surface air temperature (K), cc is cloud fraction, and is a correction term for cloud cover contribution (Oroud and Nasrallah, 1998). Figure 3 shows the spatial distribution of the average air temperature in January and July across the GOA.

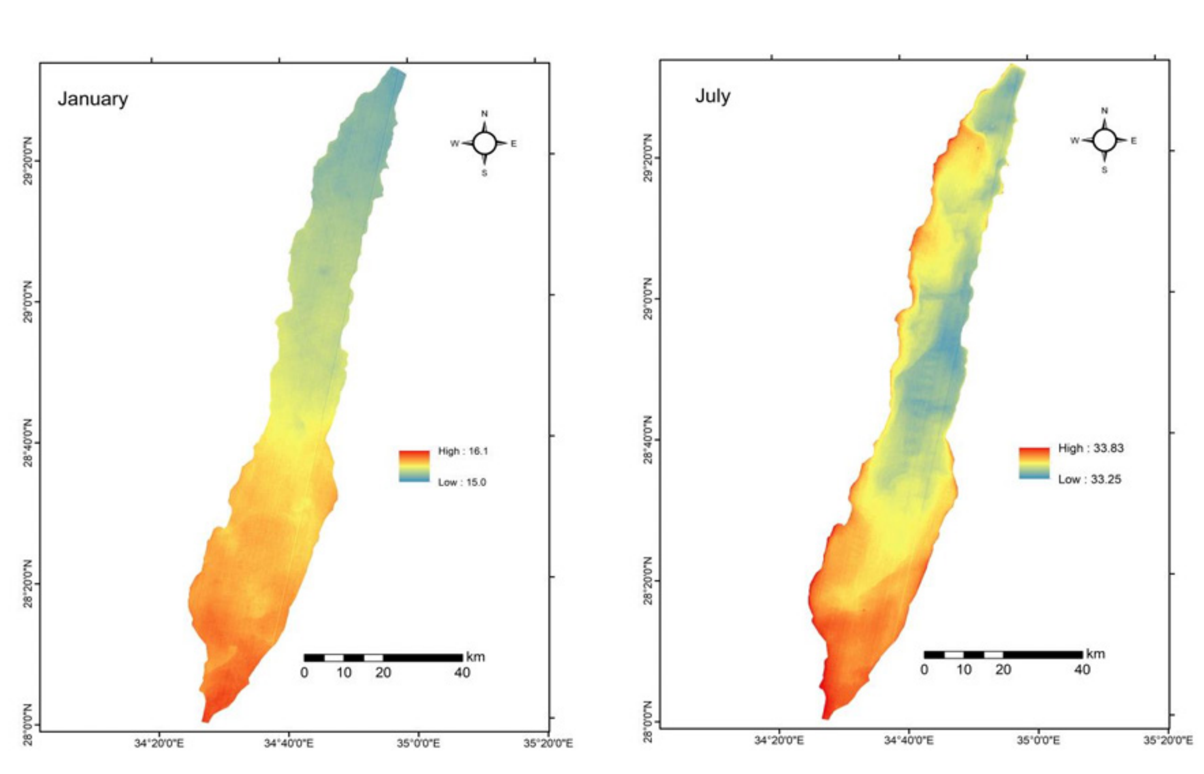

Figure 3. The spatial distribution of the average air temperature across the GOA in January and July.

The upwelling surface radiation from the sea surface is calculated using the following equation,

$$L\uparrow = \epsilon_S\, \sigma T_S^4 \tag{9}$$

where ε_s is surface emissivity, 0.97 for seawater, and T_s is surface temperature (K). Surface albedo over the GOA is assumed to be 0.05. All calculations of the various energy balance terms were performed on the raster layers using ArcGIS Pro.

The subsurface storage term is calculated assuming an effective mixed layer depth of 45 m (Oroud, 1997; Biton and Gildor, 2011),

$$QS = \rho_W\, C_W \frac{h(T_S^n - T_S^{n-1})}{\delta t} \tag{10}$$

where QS is subsurface storage (Wm^{-2}), ρw is water density (kg m^{-3}), CW is the specific heat of water (J kg^{-1} K^{-1}), h is the effective mixed layer depth (m), T_s^n and T_s^{n-1} are the surface temperature at the current and previous month, respectively, and δt is the time increment. The exact specification of the effective mixing depth does not influence the total annual evaporation as QS approaches zero for the annual cycle.

The wind function, which accounts for the aerodynamic term is expressed using the following form (Oroud, 2023),

$$F(u) = 3.6 + 2.5\, U \tag{11}$$

where U is wind speed (m s^{-1}).

The activity coefficient in Eqn. 4 accounts for the suppression of the saturation vapor pressure caused by dissolved salts. The activity of a saline solution may be expressed using the following form (Oroud, 2019a),

$$B = \frac{e_{w(Ti)}}{e_f(Ti)} \tag{12}$$

where e_w is the saturation vapor pressure of the saline solution and e_f is the saturation vapor pressure for freshwater at the same temperature. The average activity for the open seas and oceans is ~ 0.974, while it is for the GOA is ~ .97 because of its higher salinity. Water vapor pressure at the surface is calculated using the following expression (Brutsaert, 1982),

$$E_s = 6.1078 \exp^{\left(17.269 \frac{Tw}{237.3 + Tw}\right)} \tag{13}$$

where Tw is surface water temperature in Celsius. The near-surface vapor pressure is calculated by (ea* RH), where the first term is the saturation vapor pressure at T_a and RH is the relative humidity.

4. Results

4.1 Retrieved temperature

An important point for further analysis is the accuracy of the retrieved surface temperature. Figure 4 displays a scatter diagram of satellite-retrieved skin temperature compared to corresponding values retrieved from the MODIS sensor.

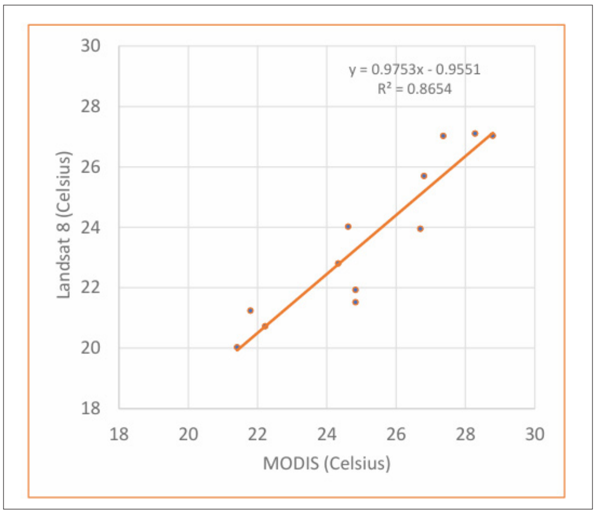

Figure 4. A scatter diagram of satellite-retrieved skin temperature versus that obtained from MODIS data.

There is close agreement between the satellite-retrieved temperatures and MODIS data, with a correlation coefficient of 0.94. Landsat 8 tends to slightly underestimate the surface temperature compared to MODIS as observed from Figure 4. This underestimation is likely linked to two main factors: 1- Landsat 8 observes the skin temperature around 10 AM when the temperature of the top water layer reaches its minimum values due to nocturnal cooling experienced the night before and the high thermal inertia of water, while the readings of MODIS are the average of observations taken at 1.00 PM and 1.00 AM. 2- MODIS data are slightly higher because of the slow heating of the upper water layer at 1.00 PM caused by the continuous flux of solar radiation and also due to the rise of the near-surface air temperature during the daytime hours. The temperature of the top layer at 1.00 AM is still warm due to the very slow cooling of water at night because the heat supplied to compensate for the net radiation deficit at night is drawn from a deep-water layer with very high heat capacity (heat capacity = $\rho_W C_W h$: see Eqn. 11). In fact, cooling at the surface layer triggers strong instability as cooled water sinks downward and gets readily replaced by warmer water from beneath. Thus, the different timing of images taken for the two satellite platforms may explain the slightly cooler temperatures of Landsat 8 compared to those obtained by MODIS. The overall accuracy, however, is quite high, and surface temperature retrieved from the high-resolution thermal images onboard Landsat 8 can be used for operational purposes in lieu of observed values to investigate surface fluxes, thereby avoiding the restrictions imposed by measurement locality and the footprints of nearby terrain.

4.2 Surface temperature across the GOA

The spatial distribution of monthly surface temperature across the GOA in six selected months, three in winter and three in summer, is presented in Figure 5. The annual surface temperature varies from an average of 20 ^{O}C in March to 27 ^{O}C in August and September. A few distinct thermal features can be identified from the figures:

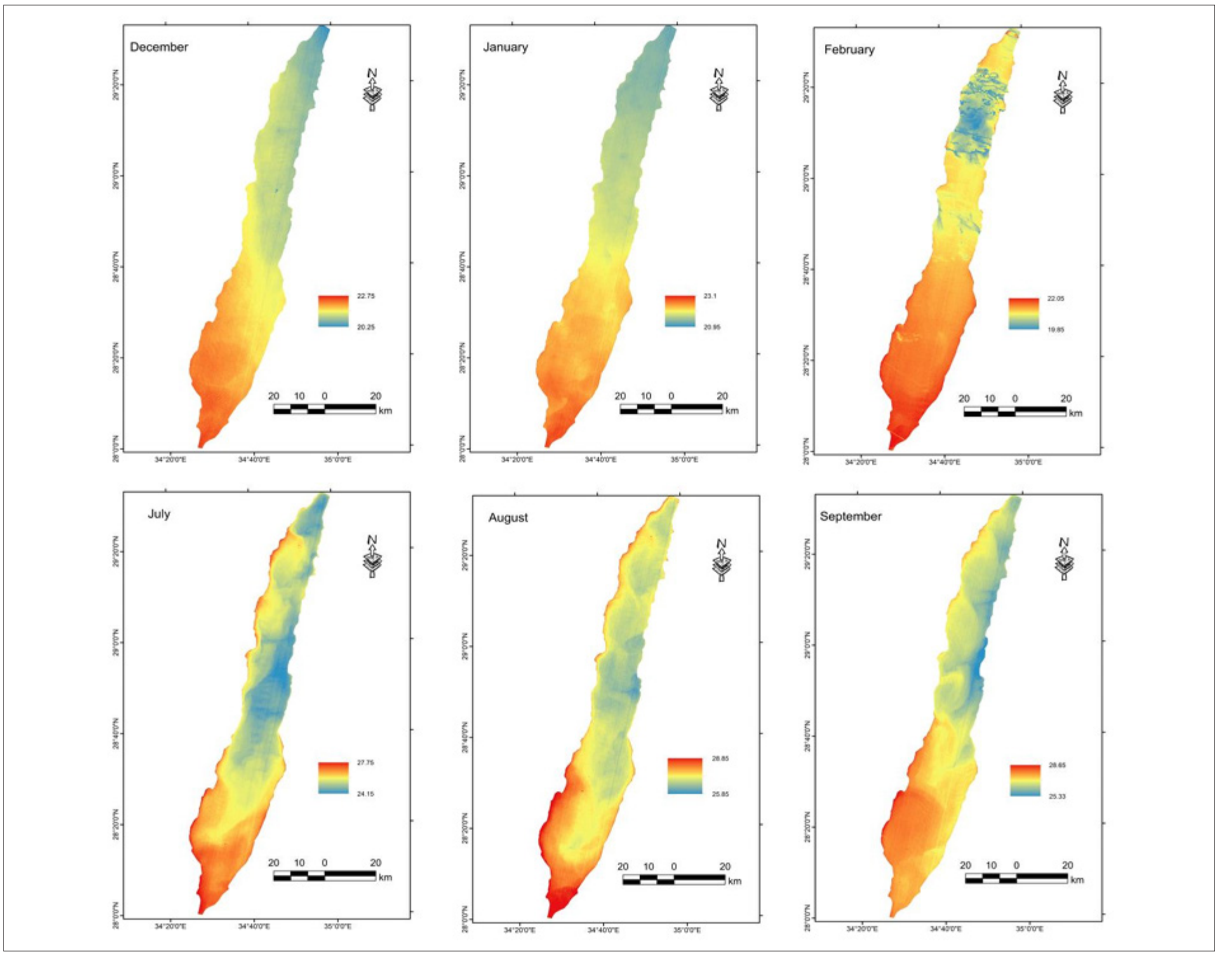

Figure 5. The spatial distribution of monthly surface temperature across the GOA in six selected months, three in winter and three in summer.

1- There is a clear north-south temperature gradient across the GOA. The temperature difference between the northern and southern parts is about 1.0-1.5 °C in winter and about 0.5 °C in summer. These seasonal differences are linked to hydrographic and meteorological forcings. Warm surface waters from the Red Sea feeding the GOA contribute to the observed warmer surface temperatures in winter in the southern parts. Furthermore, the southern parts have higher temperatures and receive more solar radiation during winter than the northern parts, as presented. Extraterrestrial radiation over the northern and southern parts of the GOA varies from about 20 MJ m^{-2} day^{-1} at the northern tip to 21.6 MJ m^{-2} day^{-1} in the southern portions in December, whereas this flux is relatively uniform across the GOA in summer (about 41 MJ m^{-2} day^{-1} in June).

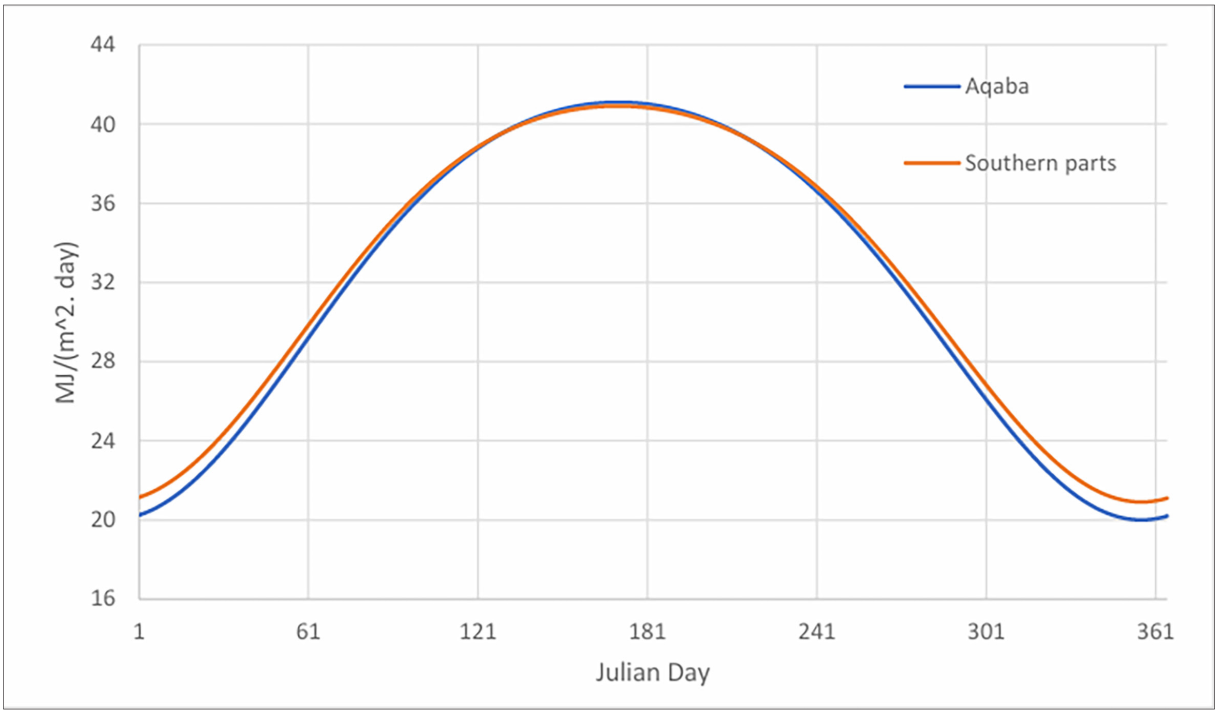

Figure 6. The annual cycle of extraterrestrial radiation over the northern and southern parts of the GOA.

2- The range of the annual SST in the GOA varies from ~5.6 ^{O}C in the southern parts to > 8 ^{O}C in the northern tip (see figure 7). This spatial temperature pattern is linked to hydrographic and atmospheric forcings. The southern parts receive a continuous flux of warm surface waters from the Red Sea, and thus the temperature there is expected to be close to that encountered over the northern Red Sea. Furthermore, solar radiation receipt over the southern portions and near-surface air temperature have less distinct annual cycles than the northern parts. The annual surface temperature range as demonstrated in Figure 7 is much smaller than those reported, for instance, in the Eastern Mediterranean- ~12 ^{O}C, the Dead Sea ~ 16 ^{O}C or the Gulf of Suez, ~ 11 ^{O}C (Berman et al., 2003; Manasrah et al. 2004; Biton and Gllord, 2011; Nykjaer, 2009; Oroud, 2019b; Oroud, 2023).

The above findings are substantiated by surface temperature retrieved from MODIS data. Figure 8 shows that the southern parts of the GOA as warmer than the northern part particularly at the end of year due to the influx of warm waters from the Red Sea, warmer air temperatures and higher solar radiation receipt as indicated in Figure 6. Landsat data provide finer details compared to the MODIS data, and thus thermal images onboard Landsat 8 are more suitable for detailed investigation of the energy balance components for small size areas like the GOA compared to coarse spatial resolution satellite platforms.

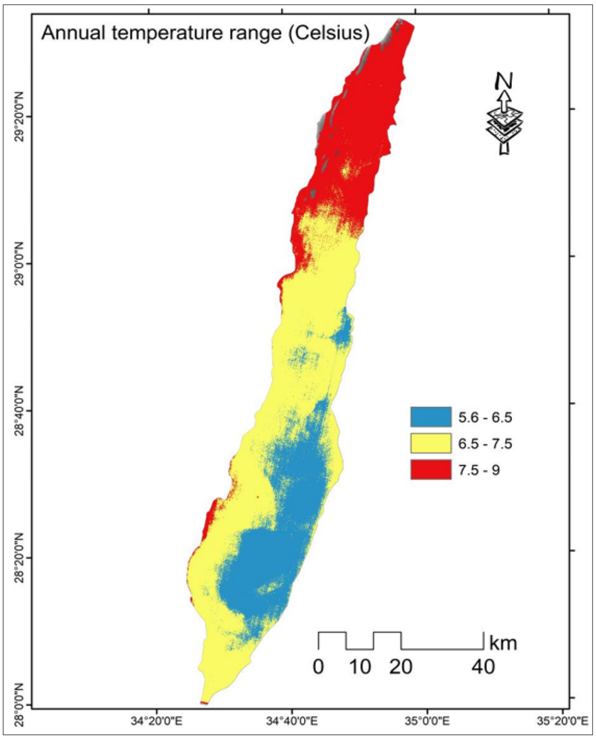

Figure 7. The annual surface temperature range across the GOA. The ST annual range is obtained by subtracting the temperature of March from that in August.

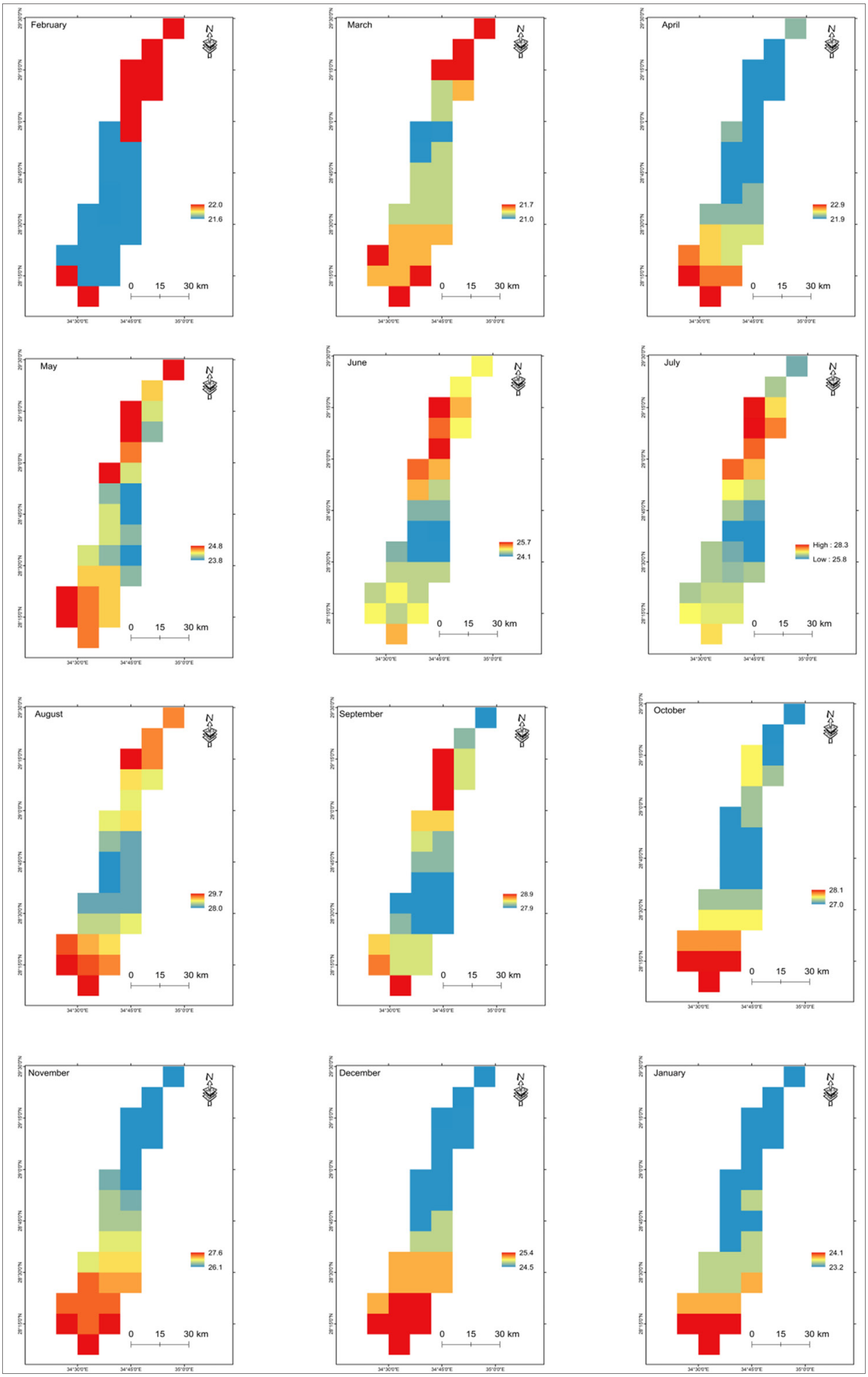

Figure 8. The spatial distribution of monthly surface temperature across the GOA as retrieved from the Moderate Resolution Imaging Spectroradiometer (MODIS) onboard the Aqua satellite during the study period.

5. Evaporation across the GOA

Evaporation across the GOA is quite high throughout the annual cycle. Figure 9 shows the spatial distribution of average daily evaporation for four selected months: two in summer and two in winter. Evaporation reaches its peak in late summer and early fall with average rates of 9.25, 10.24, and 9.57 mm day^{-1} in August, September, and October, respectively. During this period, the change in heat storage tends to be either close to zero, as in the case of August, or negative, as in the other months, and thus the available energy for evaporation is large. Despite the significant drop in air temperature and solar radiation during the low sun period, evaporation during the cold period of the year is relatively high. This pattern is due to the substantial subsurface heat release during the cooling stage of the GOA, which significantly increases available energy and thus evaporation.

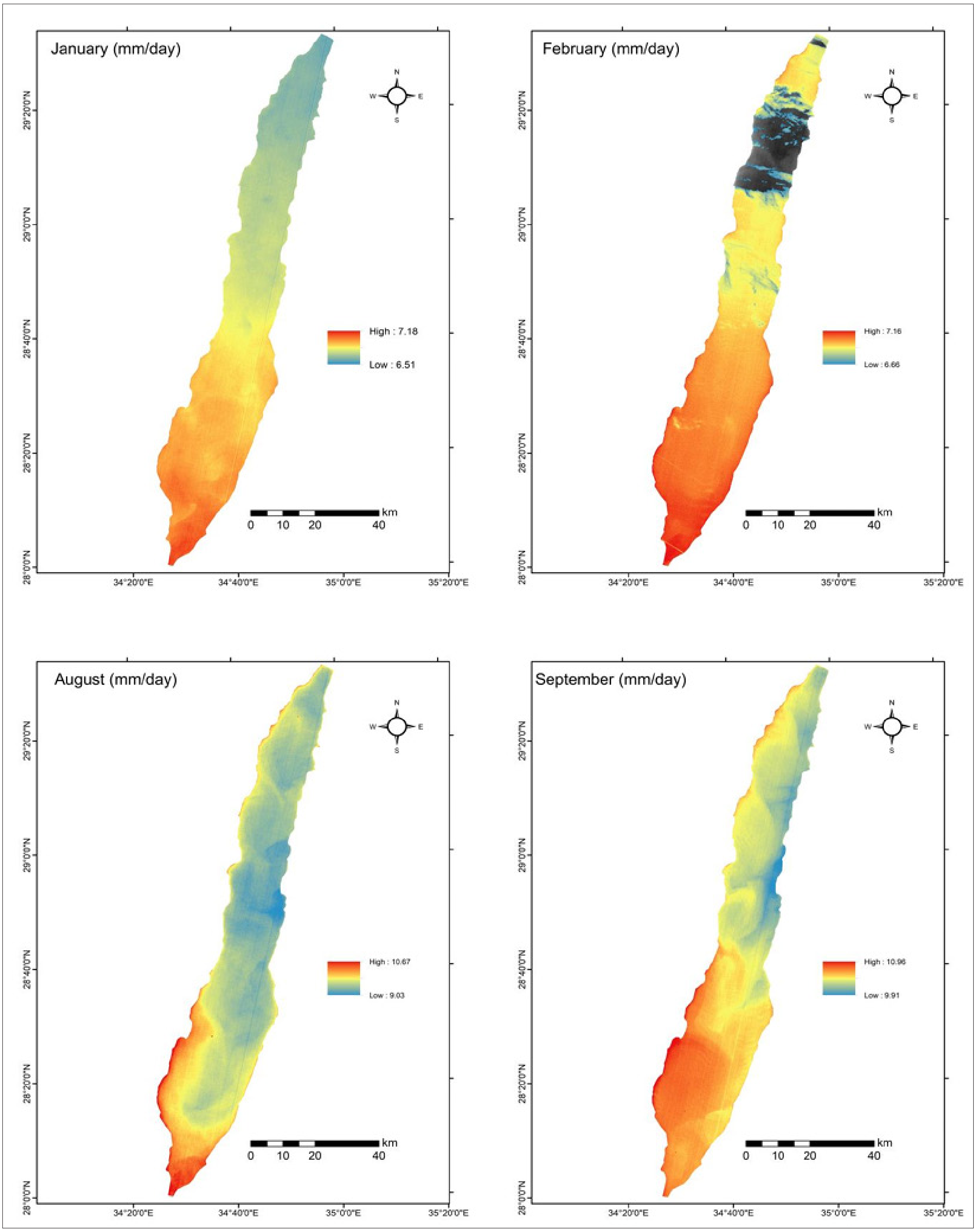

Figure 9. The spatial distribution of daily evaporation during four selected months, two in winter and two in summer.

The spatial distribution of evaporation rates from the GOA during April through September and October through March are presented in Figure 10. Average evaporation during the warm season, April through September, is 1465 mm -ranging from 1460 mm in the northern parts to 1550 mm in the southern parts-, while its counterpart in the low sun period, October through march is 1395 mm, varying from 1340 to 1450 mm across the GOA.

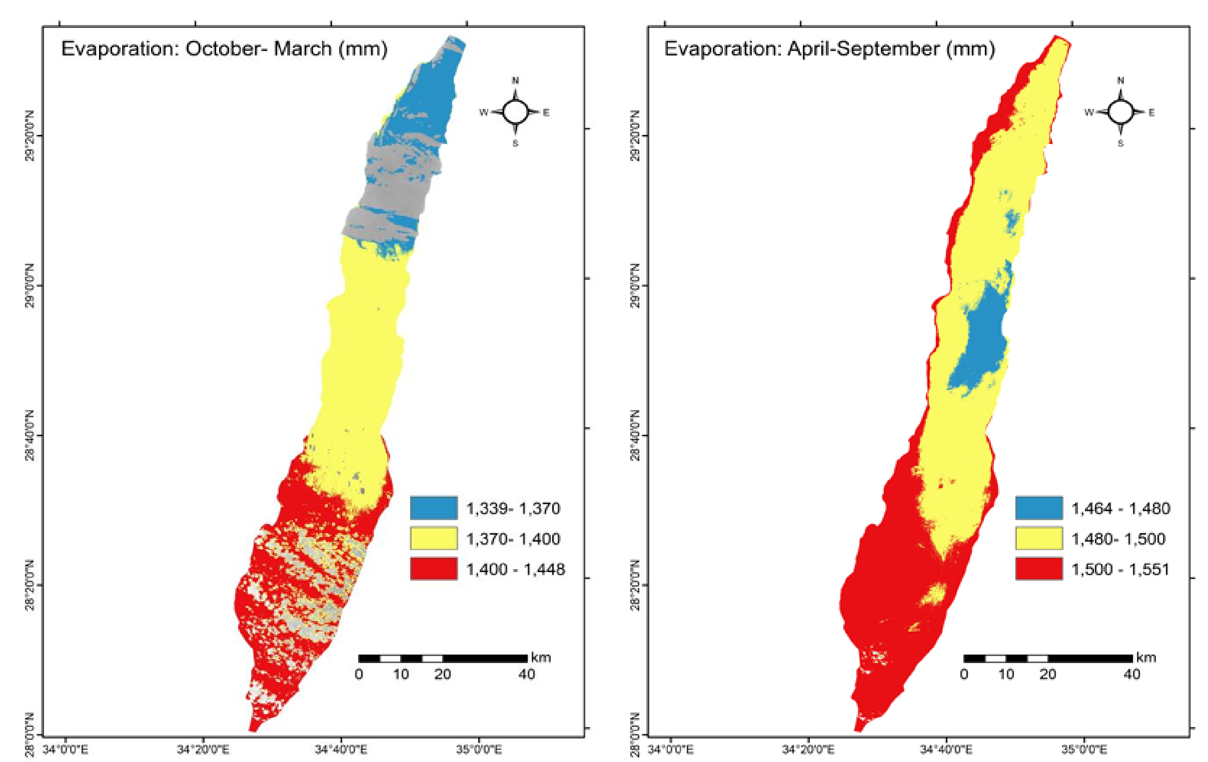

Figure 10. Total evaporation during the low sun period and the high sun period. Average evaporation for October through March is 1395 mm and the corresponding value for April through September is 1466 mm.

Although solar radiation and air temperature are relatively small in the low sun period, evaporation values across the GOA during this period are comparable to those in the warm period. This is linked to the very large subsurface heat storage during the warm period and its subsequent release in the cool period. Furthermore, the water temperature in the GOA does not vary much during the annual cycle, leading to high saturation vapor pressure deficit year-round. Evaporation across the GOA increases southward in both seasons, with the increase more pronounced from October through March.

Total evaporation across the GOA as calculated in this investigation is ~2860 mm a^{-1}. This figure is larger than those presented by da Salva (1994) and Matsoukas et al (2005; 2007), who indicated that evaporation from the Red Sea is ~1680 mm a^{-1} and ~2100-2200 mm a^{-1}, respectively. The estimates given by Matsoukas et al (2005; 2007) were based on coarse spatial resolution pixels- 2.5× 2.5 degrees. On the other hand, the calculated annual evaporation in this investigation is ~21 % lower than that reported by Assaf and Kessler (1976). Estimates presented by Assaf and Kessler were based on the bulk transfer coefficient, which is sensitive to the wind function and saturation vapor pressure deficit. Furthermore, Assaf and Kessler assumed uniform surface temperature and weather conditions throughout the GOA and neglected the effect of salinity on evaporation.

An important observation is the large contribution of the aerodynamic term in winter. The contribution of the aerodynamic term to total evaporation during the months December through March- is ~52%. On the other hand, the corresponding contribution for the period April through November is only ~ 32%, despite the larger saturation vapor pressure deficit during the warm period. Evaporation contributed by the energy term is relatively small in the cold months compared to the warm period. The physical explanation for this annual trend of energy and aerodynamic contributions is linked to the annual cycle of the energy conversion factor ($\Delta/(\Delta + \psi)$). The efficiency of the energy conversion factor increases appreciably as the temperature rises. Figure 11 shows the efficiency of the net energy conversion factor as a function of temperature. A temperature rise enhances the conversion of the available energy into evaporation but tends to suppress the aerodynamic term in the Penman equation due to the increased numerator in Eqn. 4. This tendency explains the large contribution of the energy term in the warm season and the enhanced contribution of the aerodynamic term in winter when temperature is relatively low. This tendency is expected to be larger for other locations like the Mediterranean, the Gulf of Suez or the Dead Sea due to the larger annual temperature range compared to the GOA.

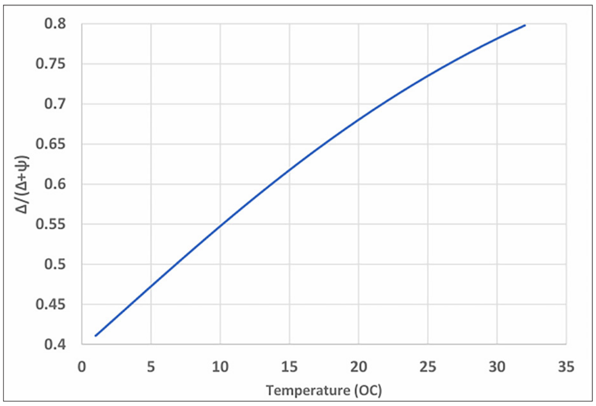

Figure 11. The efficiency of the net energy conversion factor as a function of temperature.

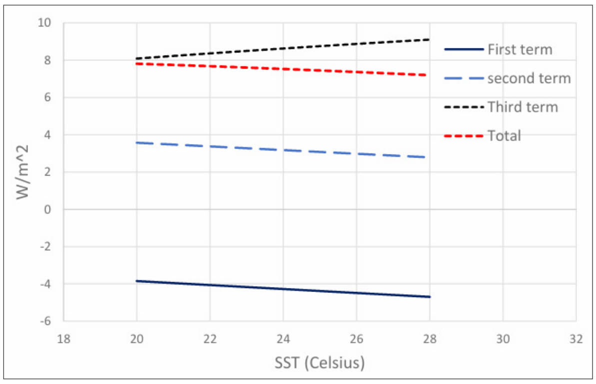

Figure 12. The sensitivity of evaporation as influenced by temperature departure at the environmental conditions encountered across the Gulf of Aqaba.

6. Sensitivity of evaporation to uncertainty in surface temperature

Surface temperature retrieved from Landsat 8 is consistent with field observations and those obtained from MODIS images, but uncertainty is expected to occur in SST which in turn influences evaporation estimates. The total effect of a temperature departure on evaporation as formulated by the Penman equation may be expressed using the following expression,

$$\frac{dE}{dT} = \frac{\partial E}{\partial Rn}\frac{\partial Rn}{\partial T} + \frac{\partial E}{\partial \Delta}\frac{\partial \Delta}{\partial T} + \frac{\partial E}{\partial e_s}\frac{\partial e_s}{\partial T} \quad (14)$$

where all terms as indicated previously. A change in temperature has positive and negative feedback effects on evaporation (Oroud, 2019a). For instance, a departure in T reduces net radiation because of the enhanced upwelling radiation, while a temperature increase elevates the saturation vapor pressure and its slope at the surface-atmosphere boundary. The effects of these mechanisms on evaporation are nonlinear.

Figure 12 shows the response of evaporation as influenced by a one Celsius temperature departure as presented in Eqn. 14 for typical meteorological conditions encountered over the GOA. Assuming that the ambient conditions are unchanged, a temperature increase has mixed effects on evaporation. For instance, a temperature increase by one Celsius at 25 ^{O}C reduces net radiation by ~6 W m^{-2} ($-4\varepsilon\sigma T^3\delta T$) but increases the saturation water vapor pressure deficit which in turn enhances evaporation flux across the surface- atmosphere boundary. Figure 12 shows that the total evaporation response caused by one Celsius departure at the environmental conditions encountered at the GOA is close to 90-100 mm/year. It is clear that a small uncertainty in SST estimates is not expected to have a large impact on the calculated annual evaporation, as presented in this investigation. Evaporation departure is indeed very small and represents only ~3% of annual evaporation. The calculated evaporation uncertainty resulting from uncertainty in SST is smaller than uncertainties caused by other terms influencing evaporation estimates, like solar radiation receipt, the wind function or incoming longwave radiation.

7. Discussion and conclusion

Accurate estimates of surface temperature are essential for numerous geophysical investigations, such as mass and heat exchange across the surface atmosphere boundary. Results show that the surface temperature of the GOA varies from a minimum of ~20 ^{O}C during the low sun period to about 27 ^{O}C in August and September. The southern parts of the GOA are warmer than the northern parts year-round. The influx of warm water from the Red Sea is likely the main mechanism influencing this spatial pattern. The warmer climate and higher solar radiation, particularly in winter, in the southern areas, also contribute to this spatial temperature gradient.

Thermal images reveal that the average annual temperature range over the GOA varies from ~5.6 °C near the Red Sea to >8 °C in the northern parts of the gulf. This spatial pattern demonstrates that the GOA does not have a uniform annual temperature range. The annual temperature range in the GOA is relatively smaller than that encountered in nearby lakes and open seas. For instance, the southeastern Mediterranean has an annual range of 12 ^{O}C while the Suez Canal, which forms the western extension of the Red Sea, was reported to have an annual temperature range close to 11 ^{O}C, and the Dead Sea has an annual temperature range in excess of 16 ^{O}C.

The annual evaporation from the GOA is quite large, reaching ~ 2860±100 mm a^{-1}. Being hyperarid and receiving no flow from nearby terrains, the large water deficit of the Gulf of Aqaba is compensated by the continuous flow of water from the Red Sea. Based on the evaporation results presented in this investigation and the area of the Gulf of Aqaba, total annual flow from the Red Sea to the Gulf of Aqaba is close to 8.86 billion cubic meters. This massive flux keeps the salinity and water temperature of the Gulf of Aqaba very close to those encountered over the northern parts of the Red Sea. This investigation provides insight into the energy, water, and salt balances across the Gulf of Aqaba, and also offers a better understanding of processes shaping the marine environment of the Gulf of Aqaba.

An important relevant point regarding the difference between Landsat and MODIS in calculating temperature and evaporation rates is illustrated. The Landsat program and the Moderate Resolution Imaging Spectroradiometer (MODIS) are widely used to estimate evaporation from both land and water surfaces, although they differ in their overpass times. Landsat is commonly applied to derive surface temperature and evaporation rates for terrestrial areas, lakes, and reservoirs, whereas MODIS sensors aboard Terra and Aqua are designed to monitor temperature and evaporation over broad regions due to their wide swath coverage. Landsat typically passes at about 10:15 a.m., while Terra and Aqua (MODIS) overpass at approximately 1:30 p.m.

Surface temperatures over land are highly sensitive to the timing of satellite overpasses because of pronounced diurnal heating cycles. In contrast, sea surface temperature shows minimal diurnal variation. This stability is primarily due to water's high thermal capacity and the involvement of a relatively deep, well-mixed surface layer generated by wave action. The large heat capacity of seawater (density × specific heat × depth) means that substantial energy is required to raise its temperature even slightly. Consequently, the precise timing of a satellite pass over has little effect on measured sea surface temperature and associated evaporation rates.

Author Declarations:

-Funding (no funding is provided)

-Conflicts of interest/Competing interests (there is no conflicting or competing interests)

-Ethics approval/declarations (not applicable)

-Consent to participate: authors agree to the conditions stipulated in the Journal guidelines

-Consent for publication (yes)

-Availability of data and material/ Data availability (data is available upon reasonable request).

-Code availability (not applicable)

References

Ahmed, A., Abou-Elhaggag, M., El-Badry, H. (2012) Hydrodynamic modeling of the Gulf of Aqaba," J. Environ. Protection, 3, (8A), 2012, 922-934. doi: 10.4236/jep.2012.328107.

Allen, R.G., Pereira, L.S., Raes, D. and Smith, M. (1998) Crop Evapotranspiration—Guidelines for Computing Crop Water Requirements. FAO Irrigation and Drainage Paper 56. Food and Agriculture Organization, Rome.

Assaf G, Kessler J. (1976) Climate and energy exchange in Gulf of Aqaba (Eilat). Mon Weather Rev 104:381–385, https://doi.org/10.1175/1520-0493(1976)104<0381:CAEEIT>2.0.CO;2

Barsi, J. A., Schottb, J. R., Palluconic F. D., Hook J. H. (2005). Validation of a Web-Based Atmospheric Correction Tool for Single Thermal Band Instruments, Earth Observing Systems X, edited by James J. Butler, Proceedings of SPIE Vol. 5882 (SPIE, Bellingham, WA, 2005), https://doi: 10.1117/12.619990

Berman, T., N. Paldor, N., Brenner, S. (2003) Annual SST cycle in the Eastern Mediterranean, Red Sea and Gulf of Elat, Geophys. Res. Lett., 30(5), 1261, https://doi:10.1029/2002GL015860.

Bernardello R, Serrano E, Coma R, Ribes M, Bahamon N (2016) A comparison of remote-sensing SST and in situ seawater temperature in near-shore habitats in the western Mediterranean Sea. Mar Ecol Prog Ser 559:21-34. https://doi.org/10.3354/meps11896

Biton, E., Gildor, H. (2011) The general circulation of the Gulf of Aqaba (Gulf of Eilat) revisited: The interplay between the exchange flow through the Straits of Tiran and surface fluxes, J. Geophys. Res., Oceans, https://doi.org/10.1029/2010JC006860

Bouwer, L., Biggs, T., Aerts, C. (2007) Estimates of spatial variation in evaporation using satellite-derived surface temperature and a water balance model, Hydrolo. Process, https://doi.org/10.1002/hyp.6636

Brutsaert, W. (1982) Evaporation into the Atmosphere. Theory, History and Application. D. Reidel Publishing Co., Dordrecht, Boston, London.

Budyko, I. (1974) Climate and Life. Academic Press.

Calder, I.R., Neal, C. (1984) Evaporation from saline lakes: a combination equation approach. Hydrol. Sci. J. 29, 89–97, https://doi.org/10.1080/02626668409490924

Cao, M., Mao, K., Yan, Y., Shi, J., Wang, H., Xu; T; Fang, S; Yuan, Z. (2021) A New Global Gridded Sea Surface Temperature Data Product Based on Multisource Data, Earth Syst. Sci. Data, https://doi.org/10.5194/essd-2021-6

Cristobal J, Jimenez-Munoz J, Prakash A, Mattar C, Skokovic D, Sobrino J. (2018) An improved single-channel method to retrieve land surface temperature from the Landsat-8 thermal band. Remote Sens 10: 431. https://doi.org/10.3390/rs10030431

da Silva, A., Young, A., Levitus, S. (1994), Atlas of Surface Marine Data 1994, vol. 1, Algorithms and Procedures, NOAA Atlas NESDIS, vol. 6, NOAA, Silver Spring, Md.

Dehwaha , A., Jadoona , K., Al-Mashharawia , S., Missimer, T. (2016) Effects of nearshore evaporation rates on the design of seabed gallery intake systems for SWRO facilities located along the Red Sea shoreline of Saudi Arabia, Desalination and Water Treatment, 57:48-49, 22726-22733, https://doi.org/10.1080/19443994.2015.1098796

Diaz, L.R.; Santos, D.C.; Käfer, P.S.; Rocha, N.S.d.; Costa, S.T.L.d.; Kaiser, E.A.; Rolim, S.B.A. (2021) Atmospheric Correction of Thermal Infrared Landsat Images Using High-Resolution Vertical Profiles Simulated by WRF Model. Environ. Sci. Proc., 8, 27. https:// doi.org/10.3390/ecas2021-10351

Faraj, T. K., Tarawneh, Q. Y., Oroud, I. M. (2022) The applicability of the tourism climate index in a hot arid environment: Saudi Arabia as a case study, International J. Env. Sci. Techno. https://doi.org/10.1007/s13762-022-04228-.

Faysash D, Smith E. (1999) Simultaneous land surface temperature- emissivity retrieval in the infrared split window. J Atmos Ocean Technol 16:1673–1689, https://doi.org/10.1175/1520-0426

Foken, T. (2008) Micrometeorology. Springer.

Folchitto, S. (1991) Seawater as salt and water source for solar ponds. Sol. Energy 46, 343–352

García-Monteiro, S., Sobrino, J.A., Julien, Y., Sòria, G., Skokovic, D. (2022) Surface Temperature trends in the Mediterranean Sea from MODIS data during years 2003–2019, Regional Studies Marine Sci., 49, doi.org/10.1016/j.rsma.2021.102086

Gristey, J.J.; Su, W.; Loeb, N.G.; Vonder Haar, T.H.; Tornow, F.; Schmidt, S.K.; Hakuba, M.Z.; Pilewskie, P.; Russell, J. (2021) Shortwave Radiance to Irradiance Conversion for Earth Radiation Budget Satellite Observations: A Review. Remote Sens. 13(13), 2640; https://doi.org/10.3390/rs13132640

Iqbal M (1983) An introduction to solar radiation. Academic, New York

Jimenez-Munoz, J.C., Sobrino J. A. (2003) A generalized single-channel method for retrieving land surface temperature from remote sensing data. J Geophys Res 108. https://doi.org/10.1029/2003JD003480

Jimenez-Munoz, J., Sobrino, J., Skokovic, D., Mattar, C., Cristobal, J. (2014). Land surface temperature retrieval methods from Landsat-8 thermal infrared sensor data. IEEE Geosci. Remote Sens. Lett. 11, 10. https://doi.org/10.1109/LGRS.2014.23120232

Kelkar, R. R. (2007) Satellite Meteorology, BS Publication, Hyderabad, India, 267 pp.

Kidd, C., Levizzani, V., Bauer, P. (2009) A review of satellite meteorology and climatology at the start of the twenty-first century, Progress in Physical Geography 33(4), 474–489 DOI: 10.1177/0309133309346647

Manasrah, R., Rasheed, M., Badran, M. (2006) Relationship between water temperature, nutrients and dissolved oxygen in the northern Gulf of Aqaba, Red Sea. Oceanologia, 48, 237–253, http://www.sciencedirect.com/journal/oceanologia

Manasrah, R., Abu-Hilal, A., Rasheed, M. (2019). Physical and Chemical Properties of Seawater in the Gulf of Aqaba and Red Sea. In: Rasul, N., Stewart, I. (eds) Oceanographic and Biological Aspects of the Red Sea. Springer Oceanography. Springer, Cham. https://doi.org/10.1007/978-3-319-99417-8_3

Matsoukas, C., Banks, A. C., Hatzianastassiou, N., Vardavas, I. (2005) The seasonal energy budget of the Mediterranean and Red Seas, Geophys. Res. Abstract, 7, 04596, https://doi.org/10.1029/2004JC002566

Matsoukas, C., Banks, A. C., Pavlakis, K. G., Hatzianastassiou, N., Stackhouse Jr, W. Vardavas, I. (2007) Seasonal heat budgets of the Red and Black seas, J. Geophys. Res., 112, C10017, https:// doi.org/10.1029/2006JC003849

Menzel, W. P. (2006). Remote sensing applications with meteorological satellites, NOAA satellite and information service, Univ. Wisconsin, Madison.

Metzger J, Nied M, Corsmeier U, Kleffmann J, Kottmeier C. (2018) Dead Sea evaporation by eddy covariance measurements vs aerodynamic, energy budget, Priestly-Taylor, and Penman estimates. Hydrol Earth Syst Sci 22:1135–1155. https://doi.org/10.5194/hess-22-1135-2018

Mundo-Molina, M., De Coss-Gomez, E. (2017) Physical-Mathematical Foundations of the Penman Equation from the Perspective of the First Law of Thermodynamics and Energy Balance Theory. Journal of Water Resource and Protection, 9, 1377-1390. https://doi.org/10.4236/jwarp.2017.912088

Neumann, J. (1952). Evaporation from the Red Sea. Israel Exploration Journal, 2(3), 153–162. http://www.jstor.org/stable/27924478

Nykjaer, L. (2009) Mediterranean Sea surface warming 1985–2006, Clim. Res., 39, 11–17, 2009 https://doi.org/10.3354/cr00794

Oroud, IM. (1997) Diurnal evaporation from fresh and hypersaline shallow ponds in a hot, dry environment. Phys Geog. 18(4):363–382, https:// doi.org/10.1080/02723646.1997.10642625

Oroud IM. (2011) Evaporation from the Dead Sea and its implications on its water balance, Theor. Appl. Climatol, 106, 523–530, https://doi.org/10.1007/S00704-0452-6.

Oroud, IM. (2018) Global warming and its implications on meteorological and hydrological drought in the southeastern Mediterranean. Environmental Processes 5, 329–348. https://doi.org/10.1007/s4071-018-0301-z.

Oroud, IM. (2019a) Evaporites: relative humidity control of primary mineral facies revisited. Hydrol. Process 33(3):395–404. https://doi.org/10.1002/HYP.13334

Oroud, IM. (2019b) The utility of thermal satellite images and land- based meteorology to estimate evaporation from large lakes. J Great Lakes Res. https://doi.org/10.1016/j.glr.2019.05.004

Oroud, IM. (2020) Spatial and temporal surface temperature patterns across the Dead Sea as investigated from thermal images and thermodynamic concepts. Theor. Appl. Climatol. 142(1–2):569–579. https://doi.org/10.1007/s00704-020-03343-9

Oroud, IM (2023) The future fate of the Dead Sea: Total disappearance or a dwarfed hypersaline hot lake? J. Hydrolo, 623, https://doi.org/10.1016/j.jhydrol.2023.129816.

Oroud, IM., Balling, R. C. (2021) The utility of combining optical and thermal images in monitoring agricultural drought in semiarid Mediterranean environments, Journal of Arid Environments, https://doi.org/10.1016/j.jaridenv.2021.104499.

Oroud, I.M. (2025) The Relative Impact of Urbanization Expansion and Climate Change on Flood Hazard in Amman City. Jordan J. Earth Environ. Sci. 2025, 1, 96–107.

Paldor N, Anati DA (1979) Seasonal variation of temperature and salinity in the Gulf of Elat (Aqaba). Deep-Sea Res 26:661–672, https://doi.org/10.1016/0198-0149(79)90039-6

Parata, A. J. (1994) Land surface temperature determination from satellites, Adv. Space Res. 14, No. 3, pp. (3)15-(3)26,

Qin, Z., Karnieli, A., Berliner, P. (2001) A mono-window algorithm for retrieving land surface temperature from Landsat TM data and its application to the Israel-Egypt border region. Int. J. Remote Sens. 22, 3729–3746, https://doi.org/10.1080/01431160010006971

Rosas, J., Houborg, R., McCabe, M. F. (2017) Sensitivity of Landsat 8 surface temperature estimates to atmospheric profile data: A study using MODTRAN in dryland irrigated systems, Remote Sens. 2017, 9, 988; https://doi.org/doi:10.3390/rs9100988

Reynolds, R. W., Chelton, D. B. (2010) Comparisons of daily sea surface temperature analyses for 2007-08. J. Climate, 23. 3545-3562, https://doi.org/10.1175/2010JCLI3294.1

Salisbury J, D'Aria D (1992) Emissivity of terrestrial materials in the 8-14 µm atmospheric window. Remote Sens Environ 42:83–106, https://doi.org/10.1016/0034-4257(92)90092-X

Sobrino, J., Jimenez-Munoz, J. (2014) Minimum configuration of thermal infrared bands for land surface temperature and emissivity estimation in the context of potential future missions. Remote Sens. Environ. 148, 158–167, https://doi.org/10.1016/j.rse.2014.03.027

Stammer, D., Wunsch, C., Giering, R., Eckert, C., Heimbach, P., Marotzke, J., Adcroft, A., Hill, C. N. and Marshall, J. (2002) The Global Ocean Circulation during 1992–1997, Estimated from Ocean Observations and a General Circulation Model. Journal of Geophysical Research, 107(27) , https://doi.org/10.1029/2001JC000888

Vonder Haar, T. H. (1994) The global energy budget and satellite observations, Advances in Space Research,14, 131-144, https://doi.org/10.1016/0273-1177(94)90362-X.

Wang, F., Qin, Z., Song, C., Tu, L., Karnieli, A., Zhao, S., 2015. An improved mono-window algorithm for land surface temperature retrieval from Landsat 8 thermal infrared sensor data. Remote Sens. 2015 (7), 4268–4289. https://doi.org/10.3390/rs70404268.

Yang, J., Gong, P., Fu, R. et al. (2013) The role of satellite remote sensing in climate change studies. Nature Clim Change 3, 875–883 (2013). doi.org/10.1038/nclimate1908.